Well-Coupled Graphene and Pd-Based Bimetallic Nanocrystals Nanocomposites for Electrocatalytic Oxygen Reduction Reaction

Huanhuan Yin,[†] Suli Liu,[†] Chunli Zhang,[†] Jianchun Bao,[†] Yulin Zheng,[†] Min Han,*[,†,‡] and Zhihui Dai*[,†]

[†]Jiangsu Key Laboratory of Biofunctional Materials, School of Chemistry and Materials Science, Nanjing Normal University, Nanjing, Jiangsu 210023, P. R. China

[‡]State Key Laboratory of Coordination Chemistry, Nanjing National Laboratory of Solid State Microstructures, Nanjing University, Nanjing, Jiangsu 210093, P. R. China

S Supporting Information

ABSTRACT: In this paper, a series of well-coupled graphene (G) and MPd_3 (M = Fe, Cu, Ag, Au, Cr, Mo, W) nanocrystals nanocomposites (G-MPd_3 NCPs) have been synthesized via a versatile electrostatic assembly and hydrogen reduction strategy, i.e., sequential assembly of coordination anions and cations on excess cationic polymer modified graphene oxide to form composite precursors and then thermal treating under H_2/Ar gases atmosphere. In those NCPs, the MPd_3 components are uniform and smaller than 10 nm, which are well anchored on G with "naked" or "clean" surfaces. By adjusting reaction temperature, the interplay of MPd_3 nanocrystals and G can be well-controlled. Below 700 °C, no sintering phenomena are observed, indicating the unprecedented dispersion and stability effect of G for MPd_3 nanocrystals. All the obtained NCPs can be directly used to catalyze oxygen reduction reaction in alkaline media. Compared with single component, monometallic, and some reported non-Pt catalysts, greatly enhanced electrocatalytic performances are observed in those NCPs due to strong synergistic or coupling of their constituents. Among them, G-$FePd_3$ NCPs exhibit the highest catalytic activity, but their current density needs to be improved compared with G-$CrPd_3$, G-$MoPd_3$, and G-WPd_3 ones. This work not only provides a general strategy for fabricating well-coupled G-MPd_3 NCPs but also paves the way for future designing multicomponent NCPs with multiple interfaces to apply in alkaline fuel cells.

KEYWORDS: graphene, bimetallic nanocrystals, nanocomposites, electrocatalysis, electrostatic assembly, hydrogen reduction
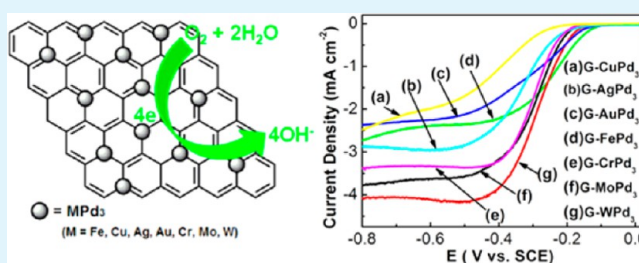
1. INTRODUCTION

Hybridization of different functional nanostructures to form multicomponent nanocrystals or heterostructural nanocomposites (NCPs) can inherit full advantages of component materials and generate enhanced or new collective properties arising from strong coupling of their components.[1] As a class of important functional nanostructures, graphene (G) composes a monolayer of sp²-hybridized carbon atoms and possesses very high surface area, excellent electrical conductivity, and mechanical properties,[2,3] which provides an ideal platform for integrating other functional nanomaterials on it to form advanced NCPs. For perfect G, only physical adsorption or weak interaction (e.g., π−π stacking) can be used to form G-based NCPs, which is disadvantageous to enhance interplay of G and other material and maximize their performances. To overcome this problem, a common strategy is to use chemically oxidized and exfoliated graphite oxide (GO) nanosheets as precursors to grow other materials and in situ reduction of GO nanosheets to obtain desired NCPs. Using this strategy, some metals (e.g., Pt, Pd, Pd−Pt),[4−6] metal oxides (e.g., Co_3O_4, Mn_3O_4, SnO_2, TiO_2),[7−10] hydroxides (e.g., $Ni(OH)_2$),[11,12] and chalcogenides (e.g., MoS_2, $SnSe_2$)[13−15] nanocrystals have been integrated on G to obtain advanced NCPs. The interplays

between desired inorganic nanocrystals and G can be enhanced to a certain degree and facilitate electronic or energy transfer. Thus, enhanced electrocatalytic, photocatalytic, photovoltaic, and energy storage performances are observed in those NCPs. Despite that great progress has been achieved in the G-based NCPs field,[16−18] there are still some limitations that need to be improved: (1) using a direct growth method; the size and shape as well as the amount or density of integrated inorganic nanocrystals are difficult to control; (2) the kinds of inorganic nanocrystals that integrate on G are limited. By far, there is no systematic study on G and bimetallic nanocrystals NCPs.

Different from the monometallic component, bimetallic nanocrystals exhibit unique optical, electronic, magnetic, and catalytic properties,[19−25] showing great promise for application in many scientific and technological fields. For instance, in electrocatalysis research, some Pd-based bimetallic nanocrystals, such as Pd−Fe,[26] Pd−Co,[27,28] Pd−Ni,[29] Pd−Cu,[30] Pd−Ag,[31,32] Pd−Mo,[33] Pd−W,[34] and so on, have shown good catalytic activity and methanol or CO tolerance ability toward

cathodic oxygen reduction reaction (ORR) in fuel cells. The component ratios and atomic distribution of Pd and other transition metals greatly affect electrocatalytic performances of desired bimetallic nanocrystals because they influence electronic coupling and transfer on the electrode surface.[35,36] Although some Pd-based bimetallic nanocrystals with different component ratios have been synthesized, there are only a few reports on MPd$_3$ type nanocrystals.[27,37,38] As is well-known, the optimal size of active metal for electrocatalytic ORR is about 3−5 nm,[39] but currently obtained Pd-based bimetallic nanocrystals are usually larger than 10 nm. Moreover, to disperse and stabilize them, the mostly used support materials are activated carbon and Vulcan XC-72 carbon,[27,33,34,40] which are easily corroded during the electrocatalytic process that leads to leaching or aggregation of the active metal component. Thus, their catalytic potentials may not be fully realized. Recently, Sun and coauthors found that G was a better supporter than the conventional carbon material, which can greatly improve electrocatalytic activity and stability of FePt nanocrystals for ORR.[41] Inspired by Sun's work and considering the current research status of Pd-based bimetallic electrocatalysts, we hybridized MPd$_3$ nanocrystals with G to form advanced NCPs and explored their applications for ORR.

Here, we report the synthesis of well-coupled G-MPd$_3$ (M = Fe, Cu, Ag, Au, Cr, Mo, W) NCPs via a general electrostatic assembly and hydrogen reduction strategy and their applications for ORR. The typical synthesis contains three steps: (1) First, GO nanosheets are prepared according to the modified Hummers' method[42] and functionalized with excess poly-(diallyldinethylammonium chloride) (PDDA) to obtain positively charged PDDA-GO; (2) By sequential assembly of coordination anions and cations on PDDA-GO, desired composite precursors containing PDDA-GO and M-Pd bimetallic complex are produced; (3) Treating the composite precursors from room temperature to 300−700 °C under H$_2$/Ar gases atmosphere, G-MPd$_3$ NCPs will be obtained. The generated MPd$_3$ nanocrystals are uniform and smaller than 10 nm, which are well dispersed on formed G with "naked" or "clean" surfaces. The density or loading amount of MPd$_3$ nanocrystals can be controlled by adjusting molar ratio of PDDA-GO and assembled bimetallic complexes. On the basis of temperature dependent experiments, the formation of MPd$_3$ nanocrystals is mainly attributed to reduction of bimetallic complexes by H$_2$, not their decomposition effect. Due to unprecedented dispersion and stabilization effect of G, no aggregation or sintering phenomena are observed at the temperature below 700 °C, beneficial to catalytic application. Electrochemical tests demonstrate that all the G-MPd$_3$ NCPs can be directly used to catalyze ORR in alkaline media, which are better than that of pure bimetallic nanocrystals, G, G-Pd, and some reported non-Pt electrocatalysts. Additionally, under identical conditions, the catalytic performances of those G-MPd$_3$ NCPs are compared. To describe briefly, G-FePd$_3$ NCPs are chosen as the example to address their synthesis, characterization, and electrocatalytic properties. While other G-MPd$_3$ NCPs will be simply discussed.

2. EXPERIMENTAL SECTION

2.1. Synthesis of G-FePd$_3$ NCPs. For each synthesis, PDDA-GO nanosheets were prepared (see Supporting Information) and used for subsequent electrostatic assembly to obtain desired composite precursors. In a typical process, presynthesized PDDA-GO nanosheets (20 mg) were dispersed in double-distilled H$_2$O (100 mL) to form a

homogeneous suspension. Then, K$_4$[Fe(CN)$_6$] (0.1 mmol) aqueous solution (10 mL) was dropped into the above suspension under vigorous stirring. After 10 min, [Pd(NH$_3$)$_4$](NO$_3$)$_2$ solution (5 mL) that was obtained by dissolving Pd(NO$_3$)$_2$ (0.3 mmol) in 25 wt % ammonia−water was rapidly added into the above mixture. By continuously stirring for 24 h, the composite precursors were obtained, which were separated and washed with water and ethanol to remove byproducts. Those composite precursors were dried in vacuum and then placed in a horizontal furnace. After introducing H$_2$ and Ar gases, the furnace was heated to 500 °C at a rate of 2 °C min^{-1} and kept at 500 °C for 1.5 h. Finally, it was naturally cooled down to room temperature. The black product was collected and used for analysis.

2.2. Synthesis of Other G-MPd$_3$ (M = Cu, Ag, Au, Cr, Mo, W) NCPs. Their synthetic procedures are similar to that for G-FePd$_3$ NCPs. The only differences are in replacing [Fe(CN)$_6$]$^{4-}$ with PdCl$_4$$^{2-}$, AuCl$_4$$^-$, CrO$_4$$^{2-}$, MoO$_4$$^{2-}$, and WO$_4$$^{2-}$ and using [Cu-(NH$_3$)$_4$]$^{2+}$, [Ag(NH$_3$)$_2$]$^+$, and [Cr(NH$_3$)$_6$]$^{3+}$ instead of [Pd(NH$_3$)$_4$]$^{2+}$, respectively.
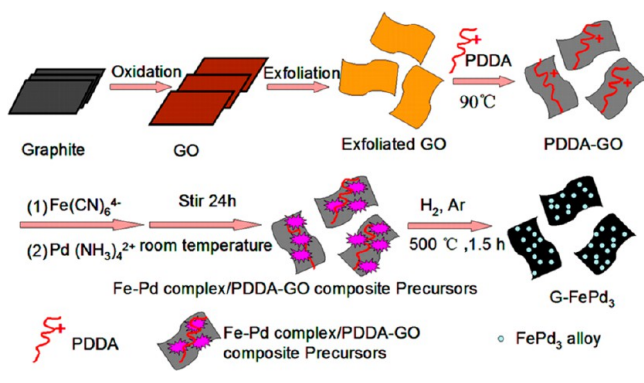
2.3. Material Characterization. The transmission electron microscopy (TEM) and high-resolution (HRTEM) images were taken on a JEOL-2100F apparatus at an accelerating voltage of 200 kV. FE-SEM images were taken on an ultrahigh resolution field emission scanning electron microscope (JSM-7600F), operating at an accelerating voltage of 10 kV. The Fourier transform infrared (FT-IR) spectra were collected on a Nexus 670 spectrometer. The thermogravimetric analysis (TGA) was performed on PERKIN-ELMER TG/DTA synchronous thermoanalysis instruments. Raman spectra were recorded on a JY HR 800 (France) instrument with an optical multichannel spectrometer Microdil 28 (Dilor) equipped with a microscope. An objective with 100× magnification was used both for focusing the excitation light (Ar$^+$ laser, 488 nm) and for collecting the scattered light. The X-ray energy dispersive spectra (EDS) were taken on a JSM-5610LV-Vantage typed energy spectrometer. Inductively coupled plasma (ICP) measurements were performed on a Jarrel-Ash 1100 + 2000 Quantometer. X-ray photoelectron spectra (XPS) were acquired on a scanning X-ray microprobe (PHI 5000 Verasa, ULAC-PHI, Inc.) using Al Kα radiation. Binding energies were calibrated using the C 1s peak (BE = 284.6 eV) as standard. The X-ray diffraction (XRD) patterns were recorded on a D/max 2500VL/PC diffractometer equipped with graphite monochromatized Cu Kα radiation (λ = 1.54060 Å) in 2θ ranging from 10 to 90°. Corresponding work voltage and current are 40 kV and 100 mA, respectively.

2.4. Electrocatalytic Measurements. Before electrocatalytic experiments, G-MPd$_3$ NCPs were dispersed in ethanol and water (4 mL, volume ratio 1:3) by ultrasonication to form a homogeneous suspension with the concentration of 2 mg mL^{-1}. Ten μL of such suspension was dropped onto pretreated glassy carbon disk electrodes (GCEs, 5 mm in diameter) by a microliter syringe. After drying in a gentle N$_2$ stream, 5 μL of 1% Nafion solution was added onto the electrode surface. Thus, G-MPd$_3$ NCPs modified GCEs were fabricated, which were used as working electrodes to perform electrochemical tests. All the experiments were carried out at room temperature on a CHI 700E electrochemical workstation (Shanghai, Chenghua Co.). A standard three-electrode system was used for all the tests. The platinum wire and saturated calomel electrode (SCE) were used as auxiliary and reference electrodes, respectively. Rotating disk voltammetry was performed on Gamry's Rotating Electrode (RDE 710) with a glassy carbon disk. All potentials in this study were reported with respect to SCE. O$_2$ reduction reactions were examined by first bubbling the electrolyte solution (0.1 M KOH) with high purity O$_2$ for 20 min and then blanketing the solution with an O$_2$ atmosphere during the entire experiment.

3. RESULTS AND DISCUSSION

The schematic diagram for the synthesis of G-FePd$_3$ NCPs is given in Scheme 1. Figure 1A shows the typical TEM image of the as-synthesized Fe−Pd complex (molar ratio of Fe and Pd is 1:3)/PDDA-GO composite precursors driven by electrostatic assembly. In contrast to "bare" GO and PDDA-GO

Scheme 1. Schematic Illustration of the Detailed Procedure for the Synthesis of G-FePd$_3$ NCPs

(Supporting Information, Figure S1), the observed black dots are the formed Fe−Pd complex, which are decorated on planar planes, edges, or wrinkle sections of light-colored thin sheets. The FE-SEM image shown in Figure 1B gives further evidence for this, from which the Fe−Pd complex (bright dots) and PDDA-GO as well as their distribution status can be well distinguished. The composition and thermal stability of those composite precursors are further examined by FT-IR and TGA. The corresponding FT-IR spectrum is shown in Figures 1C and S2, Supporting Information. For comparison, the FT-IR spectra of "bare" GO and PDDA-GO are also given. Six obvious absorption bands at 3450, 1730, 1620, 1250, 1052, and 860 cm^{-1} are found in "bare" GO, assigned to the stretching vibrations of −OH, −C=O, −COO−, −CO−H, and −C−O−C− groups.[43,44] As for PDDA-GO, the presence of asymmetric

(2924 cm^{-1}) and symmetric (2853 cm^{-1}) stretching as well as deformation vibrations of C−H for the −CH$_2$− group (1465 cm^{-1}) and stretching vibration of the C−N band (1110 cm^{-1}) confirm that PDDA has been modified on GO. The absence of characteristic peaks for epoxyl groups (1052 and 860 cm^{-1}) implies that GO has been partially reduced by PDDA.[4] Here, for expressing simply, we still name them as "PDDA-GO". While for composite precursors, two characteristic absorption bands of cyanides (−C≡N−) are observed at about 2132 and 2025 cm^{-1},[45] proving that Fe−Pd cyanide complexes have been assembled on PDDA-GO. Related TGA curves of composite precursors, bare GO, and PDDA-GO are shown in Figure 1D. At the temperatures below 150 °C, the small weight loss observed in composite precursors is attributed to removal of adsorbed water molecules or air.[46] At the 150−270 °C region, the large weight loss step may be ascribed to remove labile oxygen or other functional groups. Another weight loss step at 270−700 °C is attributed to the decomposition of the Fe−Pd complex. Although no stable platform is observed, the weight loss from 500 to 700 °C becomes unobvious, implying that the complex may be decomposed completely when the temperature exceeds 500 °C. On the basis of this result, the composite precursors are treated at 500 °C under H$_2$/Ar atmosphere to obtain desired G-FePd$_3$ NCPs.

Figure 2A,B shows the low and high magnification TEM images of obtained G-FePd$_3$ NCPs, respectively. From Figure 2A, we can see that the dense FePd$_3$ nanocrystals are uniformly dispersed or decorated on the whole surface of G. By statistic analysis, the average size of those FePd$_3$ nanocrystals is about 3.87 nm. The formation of such small-sized monodisperse FePd$_3$ nanocrystals is attributed to the presence of PDDA-GO,
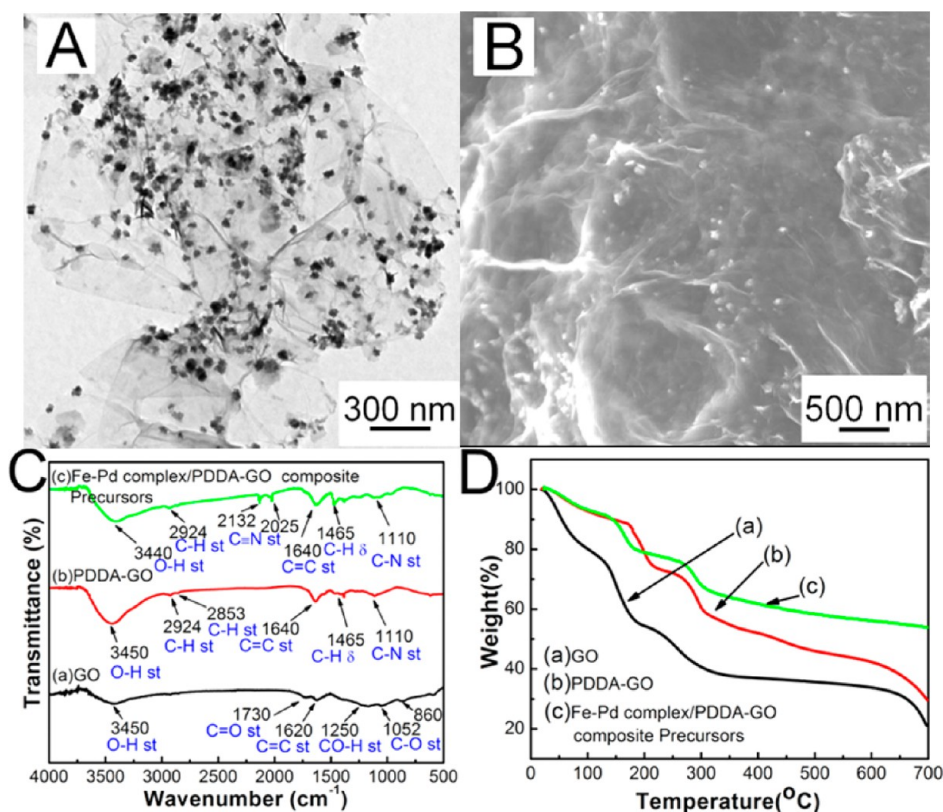

Figure 1. (A) TEM and (B) FE-SEM images of Fe−Pd complex/PDDA-GO composite precursors. (C) FT-IR spectra and (D) TGA curves of GO, PDDA-GO, and composite precursors.
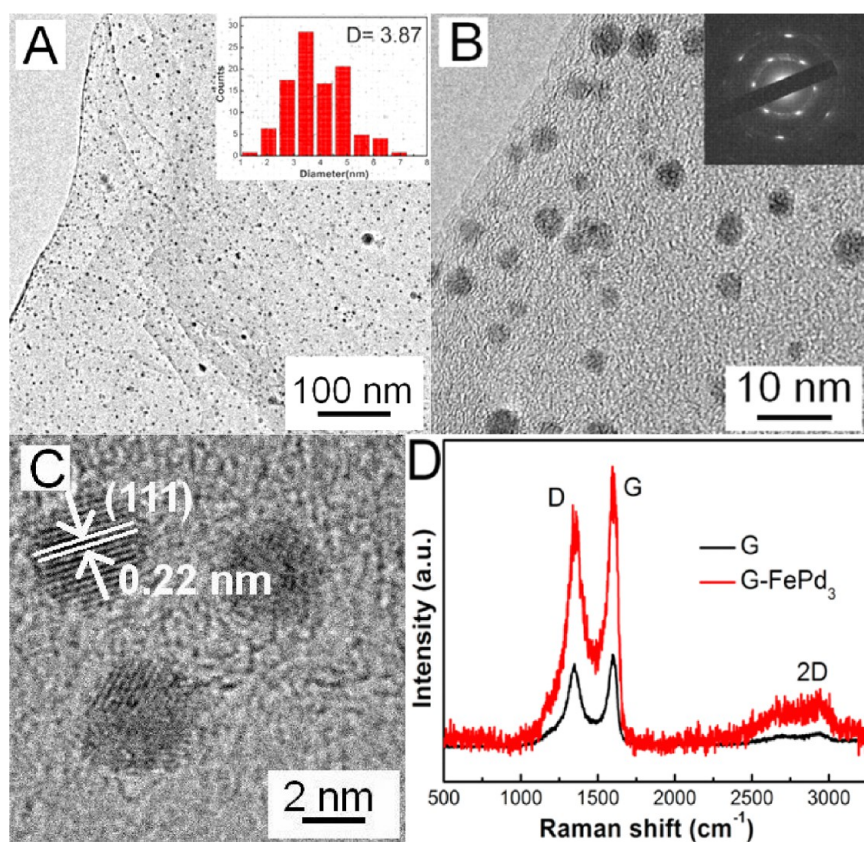
Figure 2. (A) Low and (B) high magnification TEM images of G-FePd₃ NCPs synthesized at 500 °C. (C) HRTEM image and (D) Raman spectrum of G-FePd₃ NCPs.
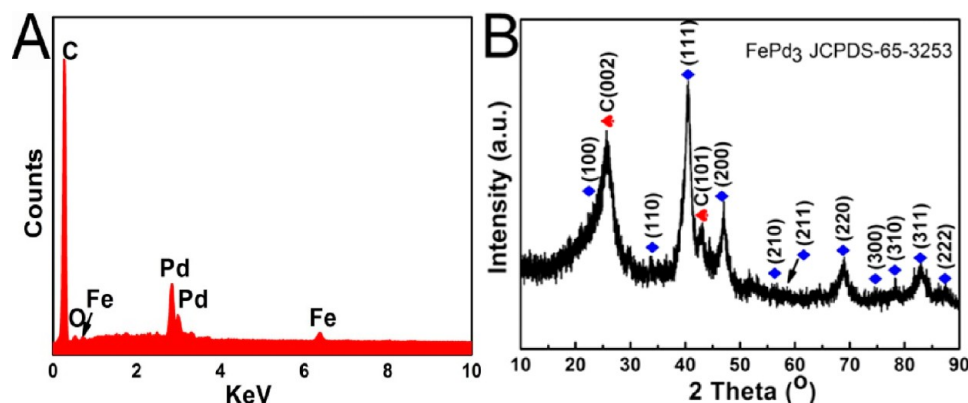

Figure 3. (A) EDS and (B) XRD patterns of G-FePd₃ NCPs synthesized at 500 °C.

which can inhibit the diffusion and collision of nanocrystals generated from the bimetallic complex. The control experiment by treating Fe−Pd complex without PDDA-GO verifies this viewpoint. Only large Fe−Pd bimetallic nanocrystals with Pd-riched ($FePd_3$) and Fe-riched ($Fe_{9.7}Pd_{0.3}$) components are generated under that case (Figure S3, Supporting Information). From the high magnification TEM image shown in Figure 2B, we can find that the $FePd_3$ nanocrystals are partially embedded into the surface of G and the clear interface between $FePd_3$ nanocrystals and G can be observed. This may give a hint that there is a strong coupling between the two components of G-$FePd_3$ NCPs, beneficial to enhance catalytic activity.[47] As illustrated in the inset of Figure 2B, the selected area electron diffraction (SAED) pattern exhibits clear spots and rings, revealing that the G-$FePd_3$ NCPs are well crystallized. A related

HRTEM image is given in Figure 2C. Besides the interfaces between $FePd_3$ and G, clear lattice fringes are observed for $FePd_3$ nanocrystals. The lattice spacing is measured to be about 2.2 Å, corresponding to interplanar separation between (111) lattice plane of cubic phase $FePd_3$ (JCPDS-65-3253). Additionally, elemental mapping analysis (Figure S4, Supporting Information) further confirms that the distribution of Fe and Pd elements is relatively uniform in $FePd_3$ nanocrystals. In order to identify the microstructure of G component in the NCPs, the Raman spectrum is further performed because it is a powerful tool for detecting ordered (sp² C, G-band) and disordered (sp³ C, D-band) crystalline structure as well as the layer number of G.[48] Figure 2D gives the Raman spectrum of G-$FePd_3$ NCPs. Two characteristic Raman peaks are observed at about 1356 and 1597 cm⁻¹, which can be assigned to D- and

G-bands of G component. In addition, a small broad peak is observed at about 2500–3000 cm^{-1} that corresponds to the 2D-band of G, revealing that the G component in the NCPs is a few layers, not a single layer.[48−50] Moreover, compared with pure G obtained by treating PDDA-GO at 500 °C in H$_2$/Ar atmosphere, the D- and G-bands of G in the NCPs are red-shifted about 2 cm^{-1} (Figure S5, Supporting Information), suggesting that there is a strong coupling of G and FePd$_3$ in obtained NCPs.[51,52]

The composition, phase structure, and crystallinity of G-FePd$_3$ NCPs are further examined by EDS, ICP, FT-IR, XPS, and XRD. Figure 3A shows the EDS spectrum of the NCPs. Except for a small O peak that originates from adsorbed air or residual oxygen-containing groups, only C, Fe, and Pd elements are detected. By integration calculation, the atomic ratio of Fe and Pd is about 1:3, which is very close to that of initial molar ratio in assembled composite precursors and consistent with ICP analysis. No N element is detected during EDS analysis, implying that Fe–Pd cyanide complex is completely decomposed or reduced at 500 °C under H$_2$/Ar gases atmosphere and N element may be converted to NH$_3$ or NO$_x$ with the carrier gas to flow out of the furnace. Further evidence comes from FT-IR (Figure S6, Supporting Information) and XPS data (Figure S7, Supporting Information). Compared with composite precursors, the FT-IR spectrum of G-FePd$_3$ NCPs exhibits no characteristic absorption bands at about 2132 and 2025 cm^{-1}, indicating the complete decomposition or reduction of Fe–Pd cyanide complex in our experiments. Additionally, the survey XPS spectrum is consistent with EDS analysis. The corresponding fine XPS spectrum for C1s proves that the initial GO has been reduced to G, and the fine XPS spectra for Fe 2p and Pd 3d confirm that the Fe–Pd complex has been reduced to bimetallic nanocrystals. From the integration area ratio of Fe 2p and Pd 3d peaks, the formed bimetallic nanocrystals can be inferred as FePd$_3$. The XRD pattern provides further evidence for this, shown in Figure 3B. In the 2θ ranging from 10° to 90°, seven obvious diffraction peaks along with six small peaks are observed. The diffraction peaks at about 23.1°, 32.8°, 40.5°, 47.2°, 53.2°, 58.8°, 68.9°, 73.9°, 78.6°, 83.1°, and 87.7° that are marked with blue rhombuses can be indexed to (100), (110), (111), (200), (210), (211), (220), (300), (310), (311), and (222) planes of cubic phase FePd$_3$ (JCPDS-65-3253). Excluding them, the two peaks at 25.6° and 43.1° labeled with red hearts are assigned to characteristic (002) and (101) planes of hexagonal graphite structure (JCPDS-65-6212) that originates from G. Because the position and intensity of the (002) diffraction peak for G is adjacent and stronger than the (100) peak of FePd$_3$, it becomes broad and asymmetric, causing only a small shoulder peak for the FePd$_3$ (100) plane to be observed. On the basis of the above analysis, we can affirm that the assembled Fe–Pd complex has been converted to FePd$_3$ nanocrystals, which are in situ anchored on G to generate well-coupled NCPs.

Theoretically speaking, thermal treating temperature will affect the size and dispersion state of the metal component as well as its coupling with G, providing good opportunities to modulate catalytic performance of desired NCPs. Therefore, except for treating at 500 °C, the composite precursors with Fe and Pd molar ratio of 1:3 are also treated at 300 and 700 °C, respectively, under H$_2$/Ar gases atmosphere. At 300 °C, the obtained product is still G-FePd$_3$ NCPs. The corresponding TEM image is shown in Figure 4A. No obvious size or morphology change is observed compared with the product
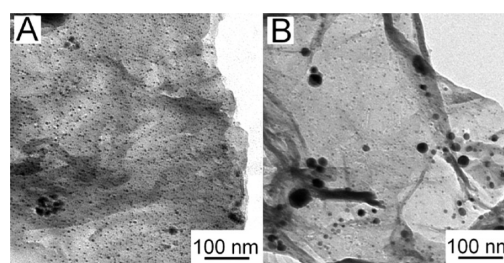

Figure 4. TEM images of G-FePd$_3$ NCPs synthesized at (A) 300 and (B) 700 °C, respectively.

synthesized at 500 °C. When this result is combined with TGA data of composite precursors, the formation of FePd$_3$ nanocrystals mainly results from reduction of Fe–Pd complex by H$_2$. It should be mentioned that the coupling of FePd$_3$ nanocrystals and G is not strong under this case. The evidence is that some FePd$_3$ nanocrystals can be isolated or exfoliated from G by treating the NCPs in an ultrasonic bath for 2 h. While at 700 °C, the size of formed FePd$_3$ nanocrystals becomes larger and some particles with a size greater than 30 nm can be found (Figure 4B). These results indicate that the optimal temperature is 500 °C for integrating monodisperse sub 10 nm FePd$_3$ nanocrystals on G to form well-coupled NCPs. Also, under optimized temperature, G-FePd and G-FePd$_2$ (Figure S8, Supporting Information) NCPs can be obtained by simply changing molar ratio of Fe and Pd in the composite precursors.

Furthermore, to verify the universality of our proposed electrostatic assembly and hydrogen reduction strategy, we further extend it to synthesize other G-MPd$_3$ NCPs. By using distinct coordination anions (e.g., PdCl$_4^{2-}$, AuCl$_4^-$, CrO$_4^{2-}$, MoO$_4^{2-}$, WO$_4^{2-}$) instead of [Fe(CN)$_6$]$^{2-}$ and using diverse coordination cations (e.g., [Cu(NH$_3$)$_4$]$^{2+}$, [Ag(NH$_3$)$_2$]$^+$, [Cr-(NH$_3$)$_6$]$^{3+}$) in place of [Pd(NH$_3$)$_4$]$^{2+}$, a series of NCPs including G-CuPd$_3$, G-AgPd$_3$, G-AuPd$_3$, G-CrPd$_3$, G-MoPd$_3$, and G-WPd$_3$ are easily obtained at 500 °C. The representative TEM and HRTEM images are shown in Figure 5 and Figure S9, Supporting Information, respectively, from which we can see that the formed MPd$_3$ products are smaller than 10 nm and well anchored on G. Corresponding XRD patterns are given in Figure S10, Supporting Information. According to Vegard law, the atomic ratios of M (M = Cu, Ag, Au, Cr, Mo, W) to Pd are calculated to be about 1:3, consistent with EDS (Figure S11, Supporting Information) and ICP measurements.

The electrocatalytic performances of G-MPd$_3$ NCPs synthesized at 500 °C are evaluated by using ORR as probe reaction. Figure 6A shows the cyclic voltammograms of G-FePd$_3$ NCPs in N$_2$- and O$_2$-saturated 0.1 M KOH solution by depositing them on a glassy carbon electrode. Compared to no noticeable reduction features between −0.8 and 0.1 V in N$_2$-saturated 0.1 M KOH solution, an obvious and strong reduction current peak can be seen with the electrolyte saturated with O$_2$, revealing the high electrocatalytic activity of G-FePd$_3$ NCPs toward ORR. Their onset reduction potential is about −0.075 V vs SCE (see Figure S12, Supporting Information), which is close or better than that of recently reported Ag-riched AgPd nanoalloy,[31] Cu nanowire-Ag NCs heterostructures,[53] Cu$_3$N nanocubes,[54] Cu$_2$Se nanowires,[55] carbon supported Co$_{1.67}$Te$_2$ nanocrystals,[56] G-Ni-α-MnO$_2$ and -Cu-α-MnO$_2$ blends,[57] and G nanoplates[58] or quantum dots.[59] To get some insight on the catalytic behaviors, the ORR

Figure 5. TEM images of (A) G-CuPd$_3$, (B) G-AgPd$_3$, (C) G-AuPd$_3$, (D) G-CrPd$_3$, (E) G-MoPd$_3$, and (F) G-WPd$_3$ NCPs, respectively.

at G-FePd$_3$ NCPs is further investigated with rotating disk voltammetry. Related polarization curves at the rotating rate of 400, 800, 1200, 1600, and 2500 rpm are shown in Figure 6B. On the basis of those polarization curves, the number of transferred electrons (n) involved in the ORR process for G-FePd$_3$ NCPs is calculated according to the following Koutecky−Levich equation:

$$\frac{1}{J} = \frac{1}{J_k} + \frac{1}{B\omega^{0.5}} \tag{1}$$

$$B = 0.62nF(D_{O2})^{2/3}v^{-1/6}C_{O2} \tag{2}$$
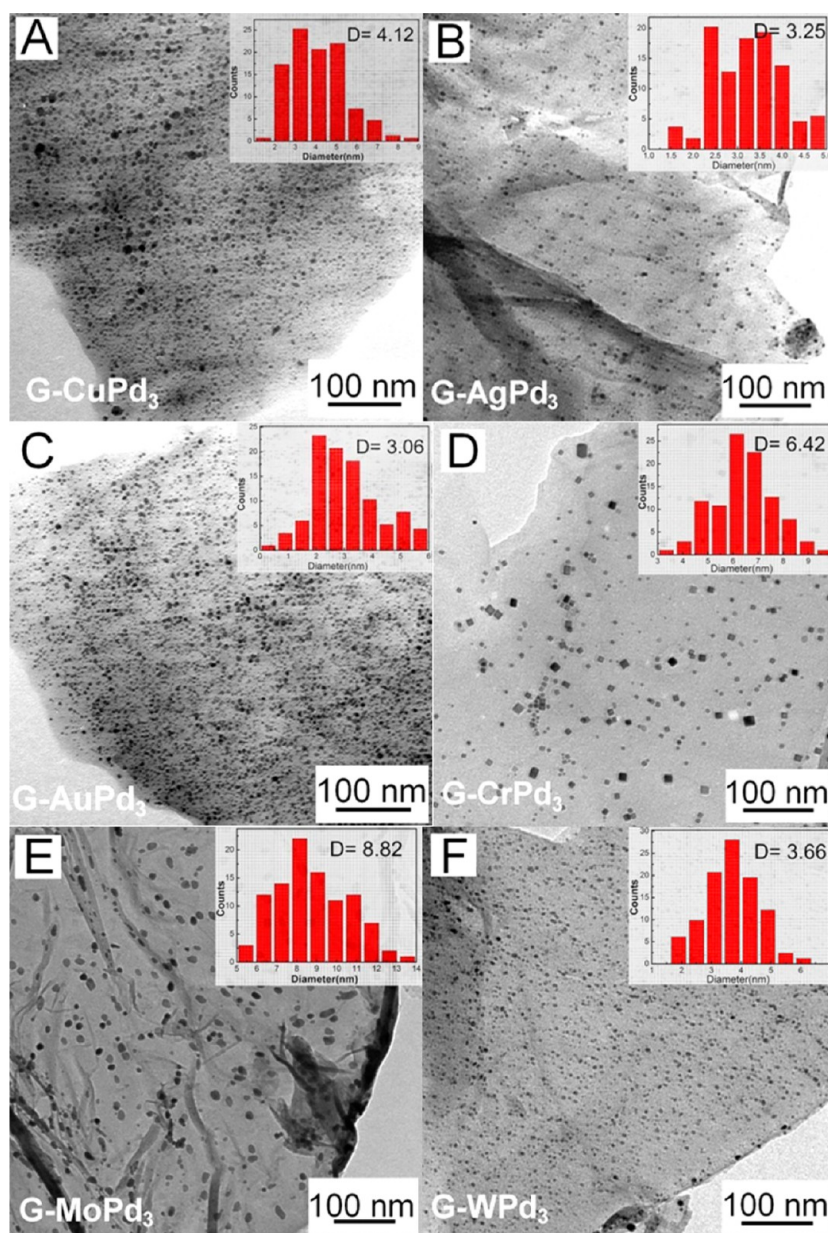
The Koutecky−Levich plots of J^{-1} vs $\omega^{-1/2}$ at a potential of −0.4, −0.5, −0.6, −0.7, and −0.8 V on G-FePd$_3$ NCPs exhibit good linearity (Figure 6C), respectively. From the slope values (1/B) of Koutecky−Levich plots, the n values for G-FePd$_3$ NCPs at −0.4, −0.5, −0.6, −0.7, and −0.8 V are calculated according to the above-mentioned formula. Corresponding

plots of n values versus potential are given in Figure 6D. At −0.4 V, the calculated n value is 3.7, which is close to 4.0. With the decrease of potential from −0.4 to −0.8 V, the n value is gradually increased. At −0.8 V, the n value reaches 4.0. Such result demonstrates that the ORR mechanism on G-FePd$_3$ NCPs mainly abides by the direct 4e$^-$ pathway (O$_2$ + 2H$_2$O + 4e$^-$ = 4 OH$^-$).[31,60] Moreover, the durability measurements reveal that there is only a little loss on current density after continuous sweeping for 5000 cycles in O$_2$-saturated 0.1 M KOH solution (Figure S13, Supporting Information), indicating the G-FePd$_3$ NCPs also possess good durability or electrocatalytic stability toward ORR.

To tentatively understand the origin for good electrocatalytic performance of G-FePd$_3$ NCPs synthesized at 500 °C, pure Fe−Pd bimetallic nanocrystals, pure G, and G-Pd NCPs (Figure S14, Supporting Information) are selected as control catalysts. Figure 7A shows their ORR polarization curves at the rotating rate of 1600 rpm. The onset reduction potentials and
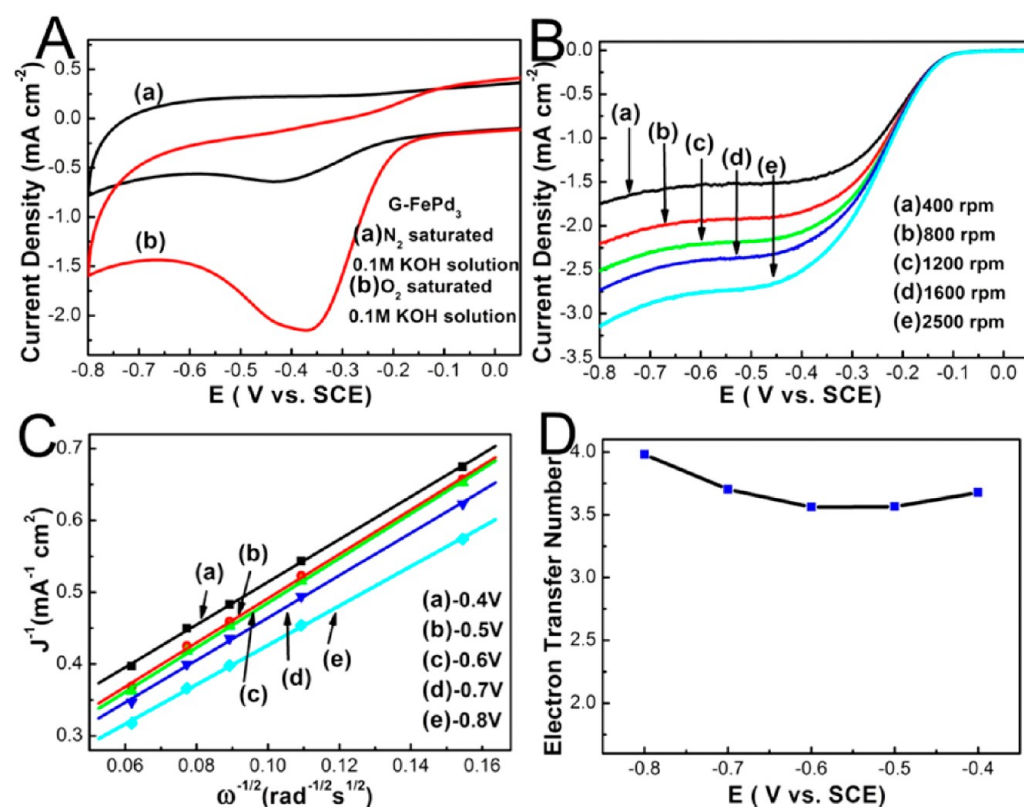
Figure 6. (A) Cyclic voltammograms of G-FePd$_3$ NCPs in N$_2$ (a) or O$_2$ (b) saturated 0.1 M KOH solution with the scan rate of 50 mV s^{-1}. (B) Rotating rate dependent ORR polarization curves for G-FePd$_3$ NCPs with the scan rate of 10 mV s^{-1}. (C) Koutecky−Levich plots of J^{-1} vs $\omega^{-1/2}$ for G-FePd$_3$ NCPs at different potential obtained from (B). (D) The plot of the number of transferred electrons versus potential for G-FePd$_3$ NCPs.
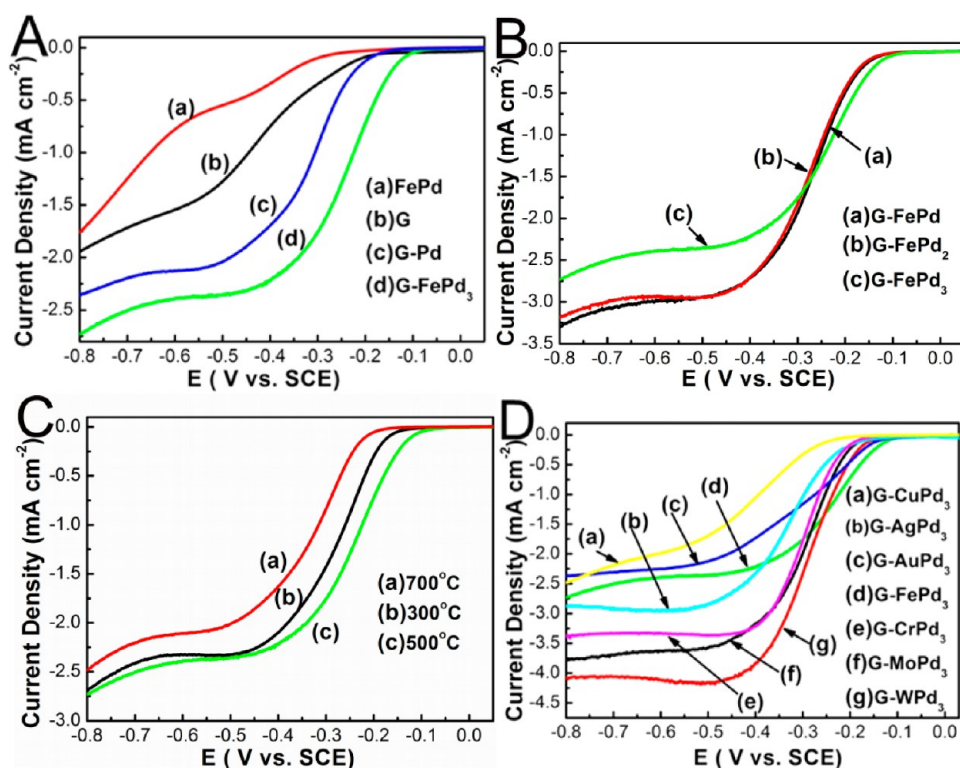

Figure 7. (A) ORR polarization curves of (a) pure Fe−Pd nanocrystals, (b) pure G, (c) G-Pd, and (d) G-FePd$_3$ NCPs. (B) ORR polarization curves of G-FePd$_x$ (x = 1, 2, 3) NCPs with different Fe and Pd molar ratios. (C) ORR polarization curves of G-FePd$_3$ NCPs obtained at different temperatures. (D) ORR polarization curves of (a) G-CuPd$_3$, (b) G-AgPd$_3$, (c) G-AuPd$_3$, (d) G-FePd$_3$, (e) G-CrPd$_3$, (f) G-MoPd$_3$, and (g) G-WPd$_3$ NCPs. The rotation rate of glassy carbon disk electrode is 1600 rpm with a scan rate of 10 mV s^{-1}.

apparent current densities of those control catalysts are more negative and much smaller than that of G-FePd$_3$ NCPs, indicating that G-FePd$_3$ NCPs possess much higher catalytic activities than single component and monometallic catalysts. Except for components, the influence of Fe and Pd molar ratios is also examined. As illustrated in Figure 7B, enhanced electrocatalytic ORR activity is observed on G-FePd$_3$ NCPs compared with G-FePd and G-FePd$_2$ ones, implying that proper Fe and Pd molar ratio is helpful to improve the performance of obtained NCPs. To observe their differences on half-wave potentials clearly, the magnified Figure 7B at the potential window of −0.6 to −0.1 V is provided in Figure S15, Supporting Information. Moreover, the G-FePd$_3$ NCPs obtained at different reaction temperature exhibit distinct catalytic performances (Figure 7C). From structural characterization data, the size and dispersion status of FePd$_3$ nanocrystals nearly have no difference for G-FePd$_3$ NCPs synthesized at 300 and 500 °C. Their diverse catalytic performance mainly originates from the differences on coupling degree of their constituents.[41,61−64] While for G-FePd$_3$ NCPs obtained at 700 °C, the size of FePd$_3$ nanocrystals becomes larger and their dispersion state turns worse, causing their catalytic performance to be greatly reduced. On the basis of the above analysis, the possible origin for good electrocatalytic performance of G-FePd$_3$ NCPs obtained at 500 °C may be as follows: (1) incorporating Fe into Pd with a proper ratio; (2) small size and good dispersion state of FePd$_3$ nanocrystals; (3) strong synergistic or coupling effect of FePd$_3$ nanocrystals and G.

Furthermore, the electrocatalytic performances of other G-MPd$_3$ (M = Cu, Ag, Au, Cr, Mo, W) NCPs synthesized at 500 °C are further studied by rotating disk voltammetry under the same mass loading and rotation rate (1600 rpm). For comparison, their ORR polarization curves along with that for G-FePd$_3$ NCPs are placed together, shown in Figure 7D. The onset reduction potentials of the NCPs containing group IB metals are found to follow the order: G-CuPd$_3$ < G-AgPd$_3$ < G-AuPd$_3$, which are more negative than that of G-FePd$_3$ ones. As for the NCPs incorporated group VIB metals, their onset reduction potentials follow the similar order: G-CrPd$_3$ < G-MoPd$_3$ < G-WPd$_3$, but they are close to that for G-FePd$_3$ NCPs. Moreover, their current density is markedly increased at the potential ranging from −0.25 to −0.8 V compared with that of G-FePd$_3$ NCPs. These results demonstrate that using G-FePd$_3$ NCPs as catalyst is better for improving onset reduction potential, while using G-CrPd$_3$, G-MoPd$_3$, and G-WPd$_3$ NCPs as catalysts are more advantageous to increase current density. Different from a previous report in which alloying Pd with Cr cannot improve electrocatalytic ORR performance,[65] our G-CrPd$_3$ NCPs exhibit greatly enhanced electrocatalytic ORR performance in alkaline media compared with G-Pd NCPs. On the basis of these results, incorporating Cr, Mo, and W elements into FePd$_3$ nanocrystals and fabricating G and trimetallic NCPs may greatly improve electrocatalytic ORR performance[66] and screen out ideal electrocatalysts for substituting conventional Pt-based ones to apply in fuel cells. Further work on this is underway.

4. CONCLUSIONS

In summary, seven kinds of well-coupled G-MPd$_3$ (M = Fe, Cu, Ag, Au, Cr, Mo, W) NCPs have been synthesized by electrostatic assembly of a specific bimetallic complex on PDDA-GO to form composite precursors and then treat them

at 300−700 °C under H$_2$/Ar gases atmosphere. In those NCPs, the active metal components are identified to be MPd$_3$ nanocrystals with cubic phase structure. They are well-dispersed on G with "naked" surfaces, and their sizes are uniform and smaller than 10 nm. The conditional experiments reveal that the formation of MPd$_3$ nanocrystals is mainly attributed to reduction of assembled bimetallic complex by H$_2$. Additionally, the interaction of MPd$_3$ nanocrystals and G can be well-controlled by adjusting reaction temperature. At the temperatures below 700 °C, no sintering phenomena are observed, which is beneficial to catalytic applications. Electrochemical tests demonstrate that all the obtained G-MPd$_3$ NCPs can be directly used to catalyze ORR in alkaline media, whose catalytic performances are better than those of pure bimetallic nanocrystals, pure G, and G-Pd control catalysts due to strong coupling of their constituents. Among them, G-FePd$_3$ NCPs exhibit the highest catalytic activity, whose onset reduction potential is more positive than other G-MPd$_3$ ones and some recently reported non-Pt electrocatalysts. Nonetheless, compared with G-CrPd$_3$, G-MoPd$_3$, and G-WPd$_3$ ones, the current density of G-FePd$_3$ NCPs needs to be improved. This work not only provides a versatile avenue for integrating sub 10 nm MPd$_3$ nanocrystals on G to form well-coupled NCPs but also paves the way for the future design of multicomponent hybrid electrocatalysts for application in alkaline fuel cells.

■ ASSOCIATED CONTENT

Ⓢ Supporting Information

Synthetic process for PDDA-GO nanosheets and G-Pd NCPs, detailed characterization of GO and PDDA-GO nanosheets as well as pure Fe−Pd bimetallic nanocrystals, FT-IR and XPS spectra of G-FePd$_3$ NCPs, TEM images and XRD patterns of G-Pd, G-FePd, and G-FePd$_2$ NCPs, HRTEM images as well as XRD and EDS patterns of other G-MPd$_3$ (M = Cu, Ag, Au, Cr, Mo, W) NCPs, and stability curve for G-FePd$_3$ NCPs. This material is available free of charge via the Internet at http://pubs.acs.org.

■ AUTHOR INFORMATION

Corresponding Authors

*Phone: +86-25-85891051. Fax: +86-25-85891051. E-mail: 07203@njnu.edu.cn (M. Han).
*Phone: +86-25-85891051. Fax: +86-25-85891051. E-mail: daizhihuii@njnu.edu.cn (Z. Dai).

Notes

The authors declare no competing financial interest.

■ ACKNOWLEDGMENTS

■ REFERENCES

(1) Wang, H. L.; Dai, H. J. Chem. Soc. Rev. 2013, 42, 3088−3113.
(2) Rao, C. N. R.; Sood, A. K.; Subrahmanyam, K. S.; Govindaraj, A. Angew. Chem., Int. Ed. 2009, 48, 7752−7777.
(3) Novoselov, K. S.; Falko, V. I.; Colombo, L.; Gellert, P. R.; Schwab, M. G.; Kim, K. Nature 2012, 490, 192−200.

(4) Zhang, S.; Shao, Y. Y.; Liao, H. G.; Engelhard, M. H.; Yin, G. P.; Lin, Y. H. *ACS Nano* **2011**, *5*, 1785−1791.

(5) Chen, X. M.; Wu, G. H.; Chen, J. M.; Chen, X.; Xie, Z. X.; Wang, X. R. *J. Am. Chem. Soc.* **2011**, *133*, 3693−3695.

(6) Guo, S. J.; Dong, S. J.; Wang, E. K. *ACS Nano* **2010**, *4*, 547−555.

(7) Liang, Y. Y.; Li, Y. G.; Wang, H. L.; Zhou, J. G.; Wang, J.; Regier, T.; Dai, H. J. *Nat. Mater.* **2011**, *10*, 780−786.

(8) Lee, J. W.; Hall, A. S.; Kim, J.-D.; Mallouk, T. E. *Chem. Mater.* **2012**, *24*, 1158−1164.

(9) Zhang, L. S.; Jiang, L. Y.; Yan, H. J.; Wang, W. D.; Wang, W.; Song, W. G.; Guo, Y. G.; Wan, L. J. *J. Mater. Chem.* **2010**, *20*, 5462−5467.

(10) Anandan, S.; Rao, T. N.; Sathish, M.; Rangappa, D.; Honma, I.; Miyauchi, M. *ACS Appl. Mater. Interfaces* **2013**, *5*, 207−212.

(11) Yan, J.; Fan, Z. J.; Sun, W.; Ning, G. Q.; Wei, T.; Zhang, Q.; Zhang, R. F.; Zhi, L. J.; Wei, F. *Adv. Funct. Mater.* **2012**, *22*, 2632−2641.

(12) Li, B. J.; Cao, H. Q.; Shao, J.; Zheng, H.; Lu, Y. X.; Yin, J. F.; Qu, M. Z. *Chem. Commun.* **2011**, *47*, 3159−3161.

(13) Li, Y. G.; Wang, H. L.; Xie, L. M.; Liang, Y. Y.; Hong, G. S.; Dai, H. J. *J. Am. Chem. Soc.* **2011**, *133*, 7296−7299.

(14) Cao, X.; Shi, Y.; Shi, W.; Rui, X.; Yan, Q.; Kong, J.; Zhang, H. *Small* **2013**, *9*, 3433−3438.

(15) Choi, J.; Jin, J.; Jung, I. G.; Kim, J. M.; Kim, H. J.; Son, S. U. *Chem. Commun.* **2011**, *47*, 5241−5243.

(16) Xiang, Q. J.; Yu, J. G.; Jaroniec, M. *Chem. Soc. Rev.* **2012**, *41*, 782−796.

(17) Lightcap, I. V.; Kamat, P. V. *Acc. Chem. Res.* **2013**, *46*, 2235−2243.

(18) Tan, C. L.; Huang, X.; Zhang, H. *Mater. Today* **2013**, *16*, 29−36.

(19) Huang, X. Q.; Tang, S. H.; Liu, B. J.; Ren, B.; Zheng, N. F. *Adv. Mater.* **2011**, *23*, 3420−3425.

(20) Cui, C. H.; Yu, J. W.; Li, H. H.; Gao, M. R.; Liang, H. W.; Yu, S. H. *ACS Nano* **2011**, *5*, 4211−4218.

(21) Kim, J. M.; Rong, C. B.; Liu, J. P.; Sun, S. H. *Adv. Mater.* **2009**, *21*, 906−909.

(22) Wang, D. S.; Li, Y. D. *Adv. Mater.* **2011**, *23*, 1044−1060.

(23) Yin, A. X.; Min, X. Q.; Zhu, W.; Liu, W. C.; Zhang, Y. W.; Yan, C. H. *Chem.—Eur. J.* **2012**, *18*, 777−782.

(24) Choi, S. I.; Xie, S. F.; Shao, M. H.; Odell, J. H.; Lu, N.; Peng, H. C.; Protsailo, L.; Guerrero, S.; Park, J. H.; Xia, X. H.; Wang, J. G.; Kim, M. J.; Xia, Y. N. *Nano Lett.* **2013**, *13*, 3420−3425.

(25) Mazumder, V.; Chi, M.; Mankin, M. N.; Liu, Y.; Metin, O.; Sun, D.; More, K. L.; Sun, S. H. *Nano Lett.* **2012**, *12*, 1102−1106.

(26) Zhang, Z. Y.; More, K. L.; Sun, K.; Wu, Z. L.; Li, W. Z. *Chem. Mater.* **2011**, *23*, 1570−1577.

(27) Wang, D. L.; Xin, H. L.; Wang, H. S.; Yu, Y. C.; Rus, E.; Muller, D. A.; DiSalvo, F. J.; Abruña, H. D. *Chem. Mater.* **2012**, *24*, 2274−2281.

(28) Lee, K. R.; Jung, Y.; Woo, S. I. *ACS Comb. Sci.* **2012**, *14*, 10−16.

(29) Sanchez, G. R.; Madeira, H. Y.; Feria, O. S. *Int. J. Hydrogen Energy* **2008**, *33*, 3596−3600.

(30) Kariuki, N. N.; Wang, X. P.; Mawdsley, J. R.; Ferrandon, M. S.; Niyogi, S. G.; Vaughey, J. T.; Myers, D. J. *Chem. Mater.* **2010**, *22*, 4144−4152.

(31) Slanac, D. A.; Hardin, W. G.; Johnston, K. P.; Stevenson, K. J. *J. Am. Chem. Soc.* **2012**, *134*, 9812−9819.

(32) Liu, M. M.; Lu, Y. Z.; Chen, W. *Adv. Funct. Mater.* **2013**, *23*, 1289−1296.

(33) Sarkar, A.; Murugan, A. V.; Manthiram, A. *J. Phys. Chem. C* **2008**, *112*, 12037−12043.

(34) Sarkar, A.; Murugan, A. V.; Manthiram, A. *J. Mater. Chem.* **2009**, *19*, 159−165.

(35) Hong, J. W.; Kim, D.; Lee, Y. W.; Kim, M.; Kang, S. W.; Han, S. W. *Angew. Chem., Int. Ed.* **2011**, *123*, 9038−9042.

(36) Liu, S. L.; Zhang, C.; Yuan, L.; Bao, J. C.; Tu, W. W.; Han, M.; Dai, Z. H. *Part. Part. Syst. Charact.* **2013**, *30*, 549−556.

(37) Shao, M. H.; Sasaki, K.; Adzic, R. R. *J. Am. Chem. Soc.* **2006**, *128*, 3526−3527.

(38) Shao, M. H.; Liu, P.; Zhang, J. L.; Adzic, R. *J. Phys. Chem. B* **2007**, *111*, 6772−6775.

(39) Guo, S. J.; Zhang, S.; Sun, S. H. *Angew. Chem., Int. Ed.* **2013**, *52*, 8526−8544.

(40) Zhang, S.; Shao, Y. Y.; Liao, H. G.; Liu, J.; Aksay, I. A.; Yin, G. P.; Lin, Y. H. *Chem. Mater.* **2011**, *23*, 1079−1081.

(41) Guo, S. J.; Sun, S. H. *J. Am. Chem. Soc.* **2012**, *134*, 2492−2495.

(42) Hummers, W. S.; Offeman, R. E. *J. Am. Chem. Soc.* **1958**, *80*, 1339−1339.

(43) Moon, G. H.; Park, Y.; Kim, W.; Choi, W. *Carbon* **2011**, *49*, 3454−3462.

(44) Woo, S.; Lee, J.; Park, S. K.; Kim, H.; Chung, T. D.; Piao, Y. *J. Power Sources* **2013**, *222*, 261−266.

(45) Lezna, R. O.; Romagnoli, R.; de Tacconi, N. R.; Rajeshwar, K. *J. Phys. Chem. B* **2002**, *106*, 3612−3621.

(46) Shimamoto, N.; Ohkoshi, S. I.; Sato, O.; Hashimoto, K. *Inorg. Chem.* **2002**, *41*, 678−684.

(47) Yoo, E.; Okata, T.; Akita, T.; Kohyama, M.; Nakamura, J.; Honma, I. *Nano Lett.* **2009**, *9*, 2255−2259.

(48) Ferrari, A. C.; Basko, D. M. *Nat. Nanotechnol.* **2013**, *8*, 235−246.

(49) Ni, Z. H.; Yu, T.; Lu, Y. H.; Wang, Y. Y.; Feng, Y. P.; Shen, Z. X. *ACS Nano* **2008**, *2*, 2301−2305.

(50) Gao, L. B.; Ren, W. C.; Liu, B. L.; Saito, R.; Wu, Z. S.; Li, S. S.; Jiang, C. B.; Li, F.; Cheng, H. M. *ACS Nano* **2009**, *3*, 933−939.

(51) Xi, P. X.; Chen, F. J.; Xie, G. Q.; Ma, C.; Liu, H. Y.; Shao, C. W.; Wang, J.; Xu, Z. H.; Xu, X. M.; Zeng, Z. Z. *Nanoscale* **2012**, *4*, 5597−5601.

(52) Giovanni, M.; Poh, H. L.; Ambrosi, A.; Zhao, G. J.; Khezri, B.; Webster, R. D.; Pumera, M. *Nanoscale* **2012**, *4*, 5002−5008.

(53) Han, M.; Liu, S. L.; Zhang, L. Y.; Zhang, C.; Tu, W. W.; Dai, Z. H.; Bao, J. C. *ACS Appl. Mater. Interfaces* **2012**, *4*, 6654−6650.

(54) Wu, H. B.; Chen, W. *J. Am. Chem. Soc.* **2011**, *133*, 15236−15239.

(55) Liu, S. L.; Zhang, Z. S.; Bao, J. C.; Lan, Y. Q.; Tu, W. W.; Han, M.; Dai, Z. H. *J. Phys. Chem. C* **2013**, *117*, 15164−15173.

(56) Wu, G.; Cui, G. F.; Li, D. Y.; Shen, P. K.; Li, N. *J. Mater. Chem.* **2009**, *19*, 6581−6589.

(57) Lambert, T. N.; Danae, J.; Lu, W.; Limmer, S. J.; Kotula, P. G.; Thuli, A.; Hungate, M.; Ruan, G. D.; Jin, Z.; Tour, J. M. *Chem. Commun.* **2012**, *48*, 7931−7933.

(58) Jeon, I. Y.; Choi, H. J.; Jung, S. M.; Seo, J. M.; Kim, M. J.; Dai, L. M.; Baek, J. B. *J. Am. Chem. Soc.* **2013**, *135*, 1386−1393.

(59) Li, Y.; Zhao, Y.; Cheng, H. H.; Hu, Y.; Shi, G. Q.; Dai, L. M.; Qu, L. T. *J. Am. Chem. Soc.* **2012**, *134*, 15−18.

(60) Parvez, K.; Yang, S. B.; Hernandez, Y.; Winter, A.; Turchanin, A.; Feng, X. L.; Müllen, K. *ACS Nano* **2012**, *6*, 9541−9550.

(61) Ding, M. N.; Tang, Y. F.; Star, A. *J. Phys. Chem. Lett.* **2013**, *4*, 147−160.

(62) Lefèvre, M.; Proietti, E.; Jaouen, F.; Dodelet, J. P. *Science* **2009**, *324*, 71−74.

(63) Wu, G.; More, K. L.; Johnston, C. M.; Zelenay, P. *Science* **2011**, *332*, 443−447.

(64) Wang, C.; Markovic, N. M.; Stamenkovic, V. R. *ACS Catal.* **2012**, *2*, 891−898.

(65) Savadogo, O.; Lee, K.; Oishi, K.; Mitsushima, S.; Kamiya, N.; Ota, K. I. *Electrochem. Commun.* **2004**, *6*, 105−109.

(66) Zhu, H. Y.; Zhang, S.; Guo, S. J.; Su, D.; Sun, S. H. *J. Am. Chem. Soc.* **2013**, *135*, 7130−7133.